Numerical Analysis of Low-Cycle Fatigue Using the Direct Cyclic Method Considering Laser Welding Residual Stress

Miaoran Liu, Afia Kouadri-Henni, Benoît Malard

coatings

MDPI

Article

Numerical Analysis of Low-Cycle Fatigue Using the Direct Cyclic Method Considering Laser Welding Residual Stress

Miaoran Liu [1,2,*], Afia Kouadri-Henni [1,2] and Benoit Malard [3]

[1] INSA Rennes, 20 Avenue des Buttes de Coësmes, 35708 Rennes, France
[2] Laboratory of Digital Sciences of Nantes (LS2N), Team ROMAS, UMR CNRS 6004, 1 rue de la Noë, 44300 Nantes, France
[3] Le Centre Interuniversitaire de Recherche et d'Ingénierie des Matériaux (CIRIMAT), Université de Toulouse, CNRS, INPT, UPS, 4 Allée Emilie Monso, 31030 Toulouse, France
* Correspondence: miaoranliu@foxmail.com

Abstract: The sequential-coupled thermo-mechanical model and direct cyclic technique are employed to investigate laser welding and low-cycle fatigue residual stress, respectively. The effects of residual stress on fatigue properties and the relaxation behaviour are analyzed. The simulation results highlight the strong dependence of laser welding residual stress on constitutive models and how low-cycle fatigue residual stress is influenced by the initial laser welding residual stress. Furthermore, the simulation indicates that residual stress redistributes and relaxes in the weld and heat-affected zone after low-cycle fatigue. To validate the accuracy of the simulation, the neutron diffraction experiment is carried out, and the experimental data are consistent with the simulation results.

Keywords: low-cycle fatigue; constitutive model; residual stress relaxation; neutron diffraction; direct cyclic method

Citation: Liu, M.; Kouadri-Henni, A.; Malard, B. Numerical Analysis of Low-Cycle Fatigue Using the Direct Cyclic Method Considering Laser Welding Residual Stress. *Coatings* **2023**, *13*, 553. https://doi.org/10.3390/coatings13030553

Academic Editor: Christian Mitterer

Received: 3 February 2023
Revised: 15 February 2023
Accepted: 17 February 2023
Published: 4 March 2023

1. Introduction

As market competition increases, the safety and reliability of the welded structure become the focus of greater attention. Laser welding can be divided into thermal conduction and deep penetration welding, according to the power density. Deep penetration welding means that the material is heated up to its melting point during the interaction between the laser and the material. When the temperature reaches its boiling point, the material evaporates to form keyholes. The heat transfers from the inside keyholes to the outside and melts the surrounding materials. During this process, keyholes remain in a stable state [1]. The power density of deep penetration welding is higher than 10^6–10^7 W/cm^2, the penetration depth is significant and the welding speed is fast. The schematic of deep penetration welding is shown in Figure 1. Compared with arc and electron beam welding technology [2], the advantages of laser welding are well known: low heat input per unit volume, a small heat-affected zone, high welding and cooling speed, little deformation and residual stress states, etc. [3]. Furthermore, the high tensile strength and low yield strength of DP600 have attracted significant attention in the manufacturing industry [4]. These characteristics of laser welding technology and DP600 show them to be perfect choices for various fields, such as aerospace, automobile production, and shipping.

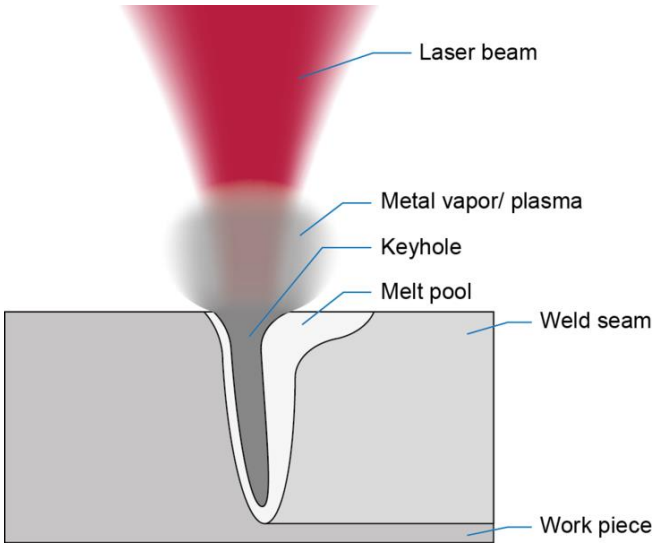

Figure 1. The schematic of melt pool shape and deep penetration welding [5].

Generally, the yield strength of the material is higher than the external stress applied to the welded structure. Neither plastic deformation nor fractures occur in the welded structure. However, when the external stress is cyclic loading, residual stress comes into play due to the superposition of stress during the use of the welded structure. Even though cyclic loading is lower than the yield strength, relaxation and fractures could be caused. Existing studies have indicated that three main factors influence the fatigue properties of the welded structure: welding residual stress, plastic deformation during the welding process and the interaction between residual stress and fatigue damages of cyclic loading. However, it is complicated to consider these factors simultaneously [6]. This paper focuses on the effects of laser welding residual stress on fatigue properties. Residual stress is internal stress that remains self-balanced in the structure after eliminating the effects of external forces or heterogenous temperature fields [7,8]. Because laser welding is a rapid heating and cooling process, thermal expansion and contraction of the welded structure is caused due to temperature gradients, resulting in residual stress. Low-cycle fatigue refers to the failure of the structure under cyclic loading close to or higher than the yield strength in less than 10^4–10^5 cycles [9]. The finite element technique is a valuable method to optimize laser welding process parameters and reveal the complex behaviors of the melt pool flow, temperature fields and stress fields during the welding process [10]. The feasibility of using numerical simulation to study the effects of residual stress on fatigue properties has been verified in publications.

Amit Kumar et al. performed dissimilar autogenous welding of ferritic/martensitic P92 steel and Inconel 617 alloy using the laser welding process. The microstructure evolution in different regions and the effects on the mechanical properties were investigated [11]. Rajiv Kumar et al. investigated the residual stress distribution in alloy 617 and 10Cr steel using finite element and deep hole drilling methods. A good correlation between the experiment and simulation was found [12]. Hossein Nassiraei et al. investigated the stress concentration factors in tubular T/Y-joints reinforced with fiber reinforced polymer and fatigue life using the finite element method [13–15].

Although the fatigue behaviors of the welded structure, taking into consideration the laser welding residual stress, have been discussed by numerous researchers, most studies have concentrated on high-cycle fatigue. Less attention has been paid to the effects of residual stress on low-cycle fatigue behaviors. This is primarily because residual stress significantly decreases under high applied stress or strain [16]. In addition, residual stress and its evolution in the low-cycle fatigue process are critical for accurately predicting fatigue life and fracture behaviour.

This paper aims to study the laser welding and low-cycle fatigue residual stress for the DP600 welded structure and the relationship between residual stress and fatigue properties, especially residual stress relaxation. Laser welding residual stress is calculated by the sequential-coupled thermo-mechanical model containing a heat source model and different plastic material constitutive models. The simulation results of laser welding residual stress are employed in the low-cycle fatigue simulation as the predefined stress field. Then, the low-cycle fatigue residual stress is obtained by the direct cyclic technique. Residual stress relaxation in the welded structure is also investigated. The results obtained from the simulation are compared with neutron diffraction results.

2. Materials

The DP600 base metal has dimensions of 180 mm × 170 mm × 1.25 mm. DP refers to the dual-phase of a ferrite matrix with good plasticity and ductility, and a martensite phase improves strength. 600 refers to the tensile strength of more than 600 MPa. The volume fraction of martensite in the ferrite matrix, between 10% and 20% [17], determines the mechanical properties of the DP600 welded structure, such as the yield strength and tensile strength. The microstructure of the DP600 welded structure is shown in Figure 2. The chemical compositions and mechanical properties of the DP600 welded structure at room temperature are shown in Tables 1 and 2. With good fatigue strength, energy absorption and strain hardening capability, DP steels are considered a superior alternative to conventional grade and high-strength low-alloy steels, and have excellent weight reduction potential, allowing the reduction of fuel consumption and greenhouse gas emissions. These desirable mechanical properties have secured the popularity of DP steels in the manufacturing industry [18].

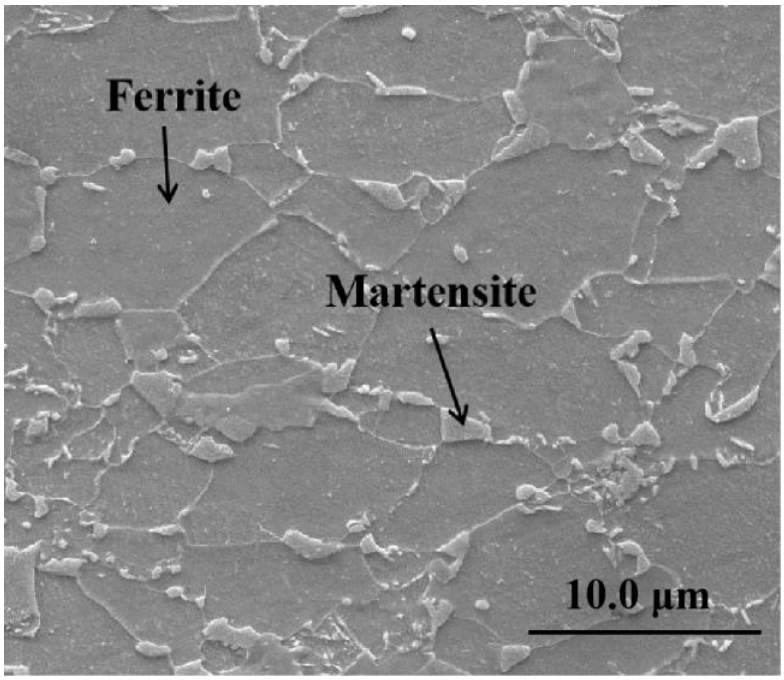

Figure 2. Microstructure of the DP600 welded structure [19].

Table 1. The main chemical compositions of DP600 in weight percentage [17].

C	Mn	P	S	Al	Cr	Si	Ni	Fe
0.10	1.09	0.03	0.001	1.19	0.02	0.26	0.01	97.20

Table 2. The main mechanical properties of DP600 [17].

Yield strength (MPa)	370 ± 40
Tensile strength (MPa)	654 ± 14
Elongation (%)	23 ± 1

3. Experiments

3.1. Laser Welding Experiment

The laser welding process is performed using the Nd: YAG laser to produce the welded joint. The laser welding machine is comprised of a 4 kW generator with an arm robot type Fanuc R2000iB. The diameter of the optical wire is 200 µm, the laser focus spot diameter is 560 µm, and the focal length is 583.5 mm, which corresponds to the focal point reference on the surface. The laser welding process is performed at a laser power of 3500 W, a welding speed of 3 m/min and a thermal efficiency of 42% with a thickness of 2.5 mm for the overlapping area and a lap joint gap of 0.1 mm. Argon is used as a shielding gas with a flow rate of 20 cubic feet per hour.

3.2. Low-Cycle Fatigue Experiment

To study the cyclic behavior of the laser welded structure, the low-cycle fatigue test machine "Instron 3369" is used and controlled by Instron software. The low-cycle fatigue experimental specimens are fabricated according to ASTM E606 [20]. During the test, the force-displacement and corresponding time are recorded. The original experimental data are then analyzed so that force-displacement curves can be converted into stress-strain curves. All the cyclic data are recorded and analyzed using the Bluehill 3 software. The low-cycle fatigue tests for the DP600 base metal and welded structure are carried out at room temperature under stress control. A sine load waveform with a stress of 400 MPa, a frequency of 5 Hz and a strain ratio of 0 is employed (Figure 3). Because the fracture is not expected to occur and the effects of fracture on residual stress are not considered, residual stress is measured after 500 cycles in this paper. The low-cycle fatigue stress-strain curve is shown in Figure 4 based on the above process parameters.

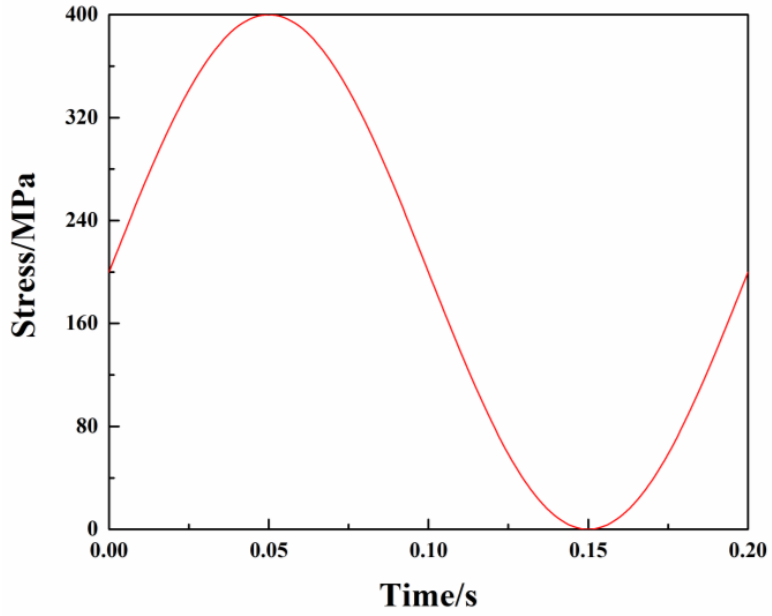

Figure 3. One cyclic loading for the low-cycle fatigue test.

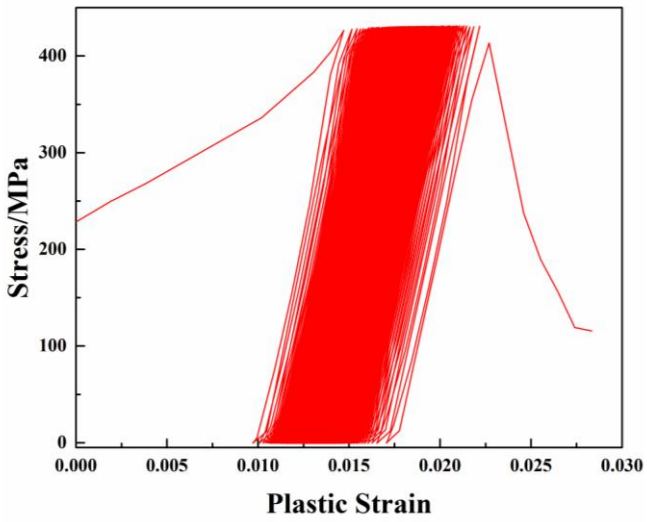

Figure 4. Cyclic stress-strain curve.

3.3. Neutron Diffraction Experiment

According to the test principle, methods for measuring residual stress can be divided into two kinds: the destructive testing method and the non-destructive testing method. The non-destructive testing method is a high-efficiency and accurate method. It works by measuring the physical properties of the material using specific equipment and then obtaining the residual stress via calculations. Through continuous improvement, it has become the essential method for measuring residual stress [21]. Diffraction methods are those most widely used among the non-destructive testing methods, including X-ray diffraction, neutron diffraction and X-ray synchrotron radiation. The neutron diffraction method was first demonstrated by Halban and Preiswerk (1936) and Mitchell and Powers (1936) showed that the neutron could indeed be diffracted by solids, following a theoretical suggestion by Elsasser (1936) that this should be possible [22]. The neutron diffraction method is used in this paper to measure the laser welding and low-cycle fatigue residual stress due to its high accuracy and excellent measurement depth advantages [23,24].

The measuremens is carried out using the dedicated SALSA diffractometer at the Institute Laue Langevin (ILL) in Grenoble. The high penetration capability of the neutron diffraction technique is used to determine the strain distribution of the ferrite phase in different directions. Due to the complex heat input in the laser welding resulting in a complex stress gradient, the base metal, the heat-affected zone and the fusion zone are scanned for residual stress measurements. On the SALSA diffractometer, the gauge volume (0.6 mm × 0.6 mm × 1 mm) is defined by the radial collimator. The neutron wavelength is set to 0.287 nm. The value of diffraction angle 2θ is equal to 93.45° for the <211> reflection and can be calculated by Equation (1) [25].

$$2\theta = 2\sin^{-1}\left(\frac{(1+v)\cdot\sin\theta_{axial}\cdot\sin\theta_{longitudinal}\cdot\sin\theta_{transversal}}{(1-v)\cdot\sin\theta_{longitudinal}\cdot\sin\theta_{transversal}+v\cdot\sin\theta_{axial}\cdot(\sin\theta_{longitudinal}+\sin\theta_{transversal})}\right) \quad (1)$$

where v is the Poisson's ratio, and θ_{axial}, $\theta_{longitudinal}$ and $\theta_{transversal}$ are diffraction angles along different normal directions. Two adjacent measurement points are placed 1 mm apart and three principal stresses are obtained for each measurement point. The experimental data are treated with Lamp software to determine residual stress and strain tensors. Figure 5 shows the dimensions for the specimens and the schematic of the experiment. Specimens 1 to 3 are used to measure the low-cycle fatigue residual stress of the welded structure, specimens 4 to 6 are used to measure the laser welding residual stress of the welded structure and specimens 7 to 9 are used to measure the low-cycle fatigue residual stress of the base metal. Tests are repeated three times to ensure the accuracy of the results.

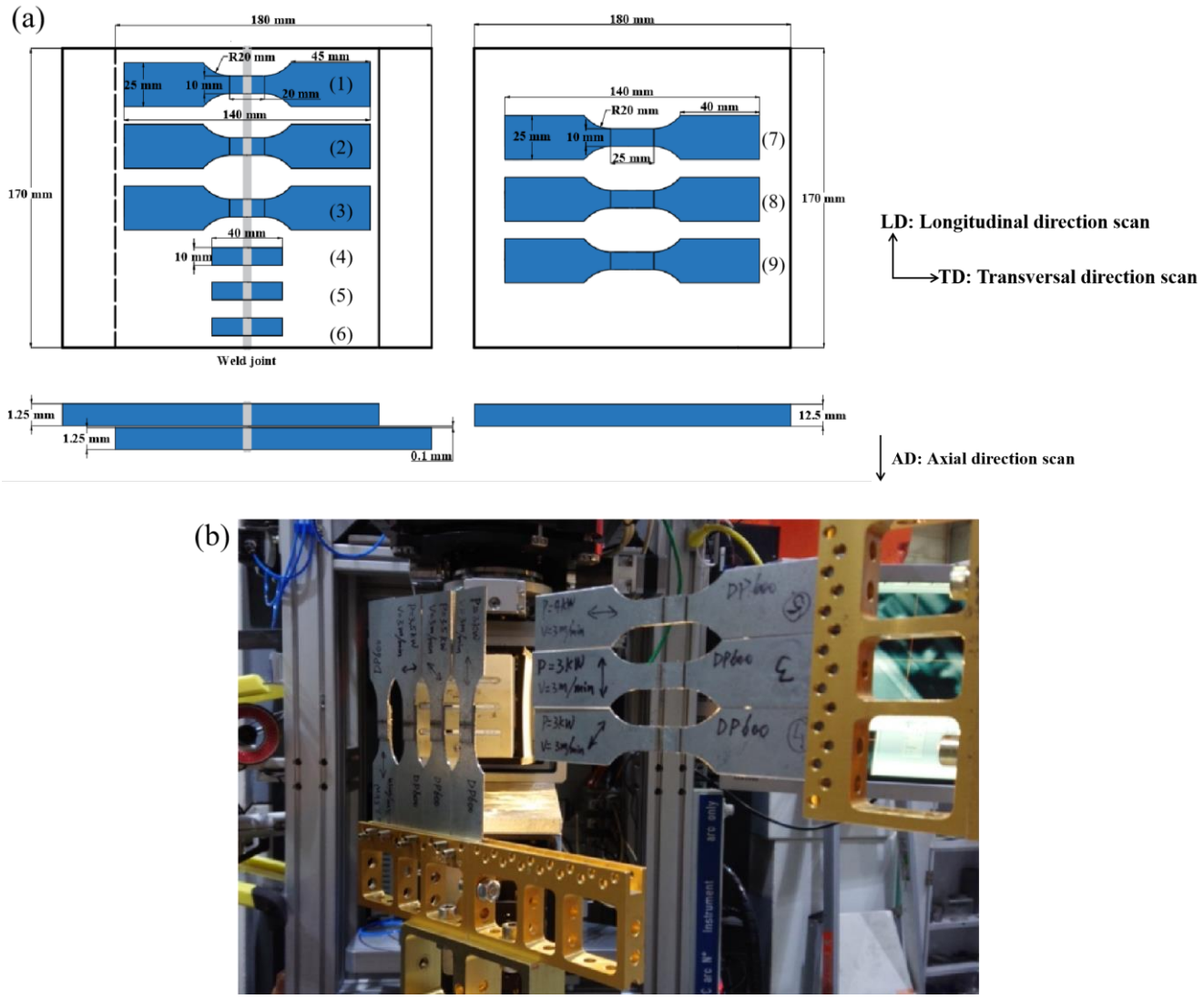

Figure 5. (**a**) Dimensions for the specimens, (**b**) schematic of the experiment.

The crystallographic texture is determined by the neutron diffraction technique on the dedicated 4-circles diffractometer 6T1 at the Laboratory Leon Brillouin (LLB). The texture shows one of the typical characteristics of DP600: slight {hlk} <211> reinforcements. However, the calculated value of the texture index is low, equal to 1.6. The <211> dependent values for Young's modulus (E_{211}) and Poisson's ratio (v_{211}) are obtained by the self-consistent elastic calculation. The result shows E_{211} ranging between 230 and 236 GPa, and v_{211} ranging between 0.27 and 0.30. These values show that the elastic anisotropy remains very low. Therefore, the elastic isotropic Hooke's law (Equation (2)) is used to calculate the triaxial residual stress from the measured strain values in this paper [26].

$$\sigma_i = \frac{E_{211}}{1+\nu_{211}}\left[\varepsilon_i + \frac{\nu_{211}}{1-2\nu_{211}}\sum_j \varepsilon_j\right] \quad (2)$$

where i and j are the longitudinal, transversal and axial, E_{211} is equal to 235 GPa and ν_{211} is equal to 0.28.

During the laser welding process, the microstructure of welded structure is changed due to rapid heating and cooling. The chemical compositions of the base metal, heat-affected zone and fusion zone are different. The type of phases in different regions depends on the temperature and the distance from the weld center. In experiments, using the

unconstrained lattice spacing of the base metal as a reference value will lead to errors in the calculation of residual stress due to the different microstructures in different regions.

Figure 6 shows the low-cycle fatigue residual stress (Von Mises) and principal stress curves along the longitudinal direction by experiment. S_{11}, S_{22} and S_{33} correspond to the normal stress in the x-direction, y-direction and z-direction, respectively. S_{12}, S_{23} and S_{13} are the sheer stress. The six stresses can be directly obtained using Abaqus finite element software. The stress measured by the neutron diffraction experiment is the principal stress. S_1, S_2 and S_3 correspond to the principal stress in the x-direction, y-direction and z-direction, respectively. The relationship among low-cycle fatigue residual stress (Von Mises), normal stress and principal stress is shown in Equation (3) [27].

$$\sigma_{VonMises} = \sqrt{\frac{(S_1 - S_2)^2 + (S_2 - S_3)^2 + (S_3 - S_1)^2}{2}} = \sqrt{\frac{(S_{11} - S_{22})^2 + (S_{22} - S_{33})^2 + (S_{33} - S_{11})^2 + 6(S_{12}{}^2 + S_{13}{}^2 + S_{23}{}^2)}{2}} \quad (3)$$

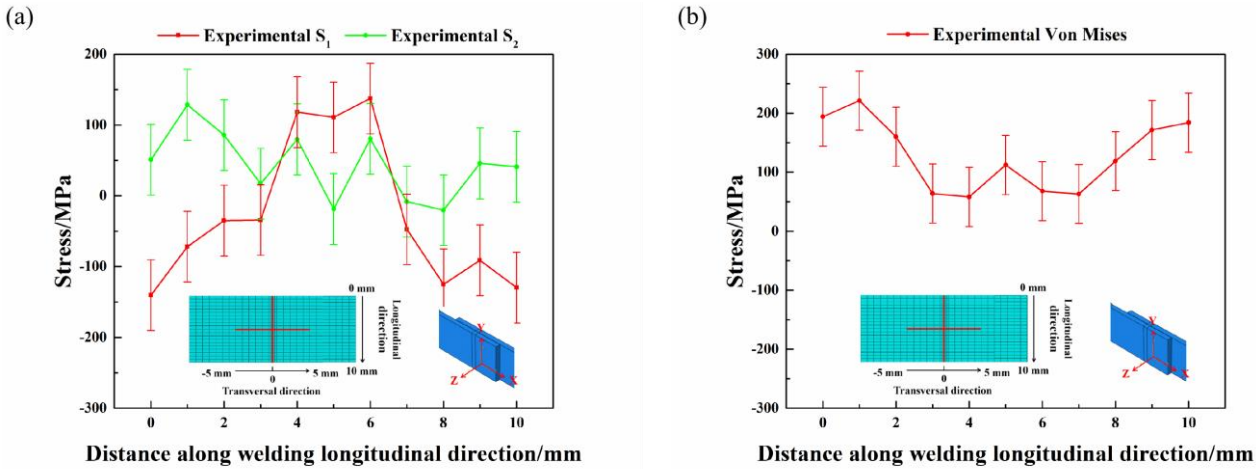

Figure 6. Low-cycle fatigue residual stress by neutron diffraction (**a**) S_1 and S_2, (**b**) Von Mises.

4. Simulations

4.1. Finite Element Model

Finite element models of the welded structure and the base metal are developed using Abaqus software. During the laser welding simulation, the temperature of the weld changes sharply and presents a highly nonlinear characteristic due to the high concentration of laser energy. Hence, the material properties change with the temperature. Temperature-dependent material properties such as thermal conductivity, specific heat, thermal expansion and mass density are considered for thermal and mechanical analysis, respectively. Temperature-dependent Young's modulus and Poisson's ratio are employed for the elastic strain calculation. Furthermore, the plastic strain is calculated using the plastic material constitutive models. The Low-cycle fatigue simulation is carried out at room temperature and the value of Young's modulus and Poisson's ratio at 25 °C are used for calculating the elastic strain. The plastic strain is calculated using the experimental data. Models with finer mesh sizes near the weld center and coarser ones away from the weld zone are used. The sensitivity of the mesh is tested by varying the mesh density in the weld zone. Optimized mesh sizes are found that ensure simulation accuracy. Due to the different analysis steps in Abaqus, two different types of elements are used for laser welding (C3D8T element type) and low-cycle fatigue (C3D8R element type) simulations. Young's modulus and Poisson's ratio at different temperatures are shown in Figure 7.

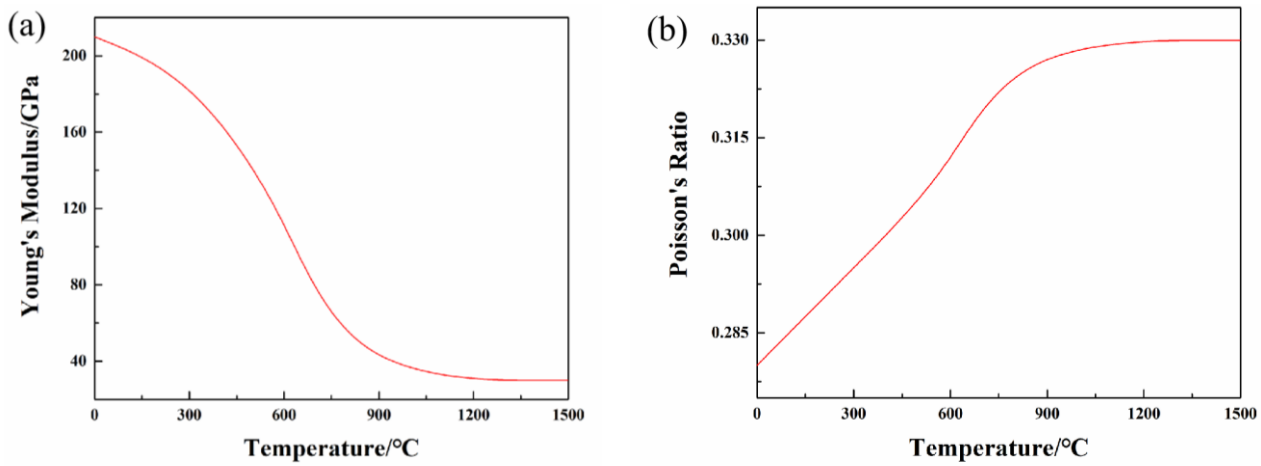

Figure 7. Elasticity of DP600 (**a**) Young's modulus, (**b**) Poisson's ratio [28].

4.2. Boundary Conditions

Boundary conditions in the thermal and mechanical analysis need be defined. The room temperature of 25 °C is used as the initial condition in both laser welding and low-cycle fatigue simulations. For the boundary conditions in thermal analysis, heat loss due to thermal conduction, convection and radiation is considered.

The welded structure is continuously heated and cooled during the movement of the heat source, that mainly exchanges heat through thermal conduction. There is thermal convection and thermal radiation between the welded structure and surrounding areas during the welding process. Thermal convection is the primary method for exchanging heat between the welded structure and the surroundings during the cooling process. Thermal conduction occurs due to temperature gradients, resulting in heat exchange. This exchange can occur between two objects with a temperature difference or inside the same object with an uneven temperature field. The thermal conduction equation is as follows [29]:

$$\rho \frac{dH}{dt} - div(\lambda gradT) - Q = 0 \tag{4}$$

where ρ is the density (kg/m^3), H is the enthalpy (J/(kg·°C)) that depends on specific heat capacity, λ is the heat conductivity (W/(m·°C)), T is the temperature (°C) and Q is the heat source density (W/m^3).

Thermal convection primarily refers to the heat exchange between the solid surface and the surrounding fluid due to temperature differences. Thermal convection and thermal conduction work together on the objects. The thermal convection equation is as follows [29]:

$$\lambda(T) gradT(x_i, t)_{surface} + h(T(x_i, t) - T_r) = 0 \tag{5}$$

where h is the thermal convection coefficient equal to 7.35×10^{-5} W/(mm^2·°C), and T_r is the room temperature (°C).

Due to the temperature, the objects continuously radiate electromagnetic waves into their surroundings. The objects absorb energy from radiation and convert it into thermal energy. This method of exchanging heat is called thermal radiation. The objects can produce thermal radiation if the temperature is higher than absolute zero (T_∞). Higher temperature leads to a higher energy level of radiation. Thermal radiation can occur without any medium and propagate in a vacuum. When the objects and their surroundings are in thermal equilibrium, the thermal radiation exchange is zero, reaching the dynamic equilibrium. The thermal radiation equation is as follows [29]:

$$\lambda(T)gradT(x_i,t)_{surface} + \varepsilon c(T(x_i,t)^4 - T_\infty{}^4) = 0 \quad (6)$$

where ε is the emissivity of the radiating surface and c is the thermal radiation coefficient equal to 2.5×10^{-7} W/(mm^2·°C).

Boundary conditions in the mechanical analysis should eliminate the rigid body displacements of the model and not affect the free deformations of the structure. This paper simulates the constraints of the welded structure to obtain results close to the actual situations.

4.3. Heat Source Model

The finite element method can effectively solve the problems of the welding process. It is necessary to employ an appropriate heat source model to reproduce the temperature and stress fields in the simulation. Otherwise, it can lead to significant differences in simulation and experimental results. The laser power, welding speed and thermal efficiency mentioned in Section 3.1 are applied to the heat source model and implemented in Abaqus using the subroutine DFLUX. The conical heat source with Gaussian distribution (Figure 8) used in this paper is characterized by the maximum heat flux at the top surface and the minimum at the bottom surface of the structure. The heat density along the z-direction is kept constant. In any plane perpendicular to the z-direction, the heat density is distributed in Gaussian distribution [30]. This heat source model helps to simulate the welding process with high energy density and obtains the weld with concentrated energy and a large aspect ratio, which is closer to the actual situations of laser self-fusion welding [31].

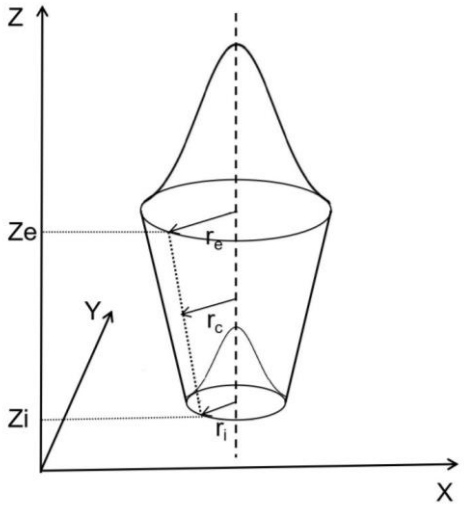

Figure 8. Conical heat source with the Gaussian distribution [31].

For a conical heat source with Gaussian distribution, if the height of the heat source is:

$$H = z_e - z_i \quad (7)$$

where z_e is the Z position of the top (2.6 mm = 2 × 1.25 mm + 0.1 mm in Figure 5a) and z_i is the Z position of the bottom (0 mm), then:

$$r_c(z) = r_e - \frac{(r_e - r_i)(z_e - z)}{z_e - z_i} \quad (8)$$

where r_c is the radius at the height of Z with linear attenuation in the thickness direction, r_e is the radius of the top (0.65 mm) and r_i is the radius of the bottom (0.5 mm), then the volume range of the heat source effect is:

$$A_v = \int_0^H {r_c}^2 \pi dh = \frac{H}{3}({r_e}^2 + r_e r_i + {r_i}^2)\pi \quad (9)$$

The Gaussian distribution has superposed a series of planar Gaussian heat sources in the thickness direction of the welded structure. The heat flux distribution of the heat source model is:

$$q_c(r,z) = \frac{3\eta pe^3}{A_v(e^3-1)} \exp\left[-\frac{3(x^2+y^2)}{{r_c}^2}\right] \quad (10)$$

where η is the efficiency (0.42) and P is the laser power (3500 W).

4.4. Direct Cyclic Method

Generally, the characterization of fatigue properties for the welded structure requires many fatigue experiments. The experimental periods are lengthy and costly, and many conditions can affect the result. In recent years, finite element software has been widely adopted to investigate the residual stress field and the evolution of laser welding and low-cycle fatigue residual stress. With the advancement of finite element technology, Abaqus has shown significant potential. It can be used to obtain accurate temperature and stress field results and eliminate the need for costly and time-consuming experiments. The most used analysis step in Abaqus is the static general step. However, it has the same disadvantage as the experiment: the huge time costs. An effective modeling technique in Abaqus, the direct cyclic step, is used to calculate low-cycle fatigue residual stress in this paper. This technique is a quasi-static analysis that combines Fourier series and time integration of the nonlinear material behavior. The stabilized responses of the structure can be obtained directly. Stabilized responses signify that the welded structure may achieve a stable state following dynamic cyclic loading in which the stress-strain relationship is the same in each subsequent cycle. The direct cyclic step effectively solves the problem of time costs resulting from the huge cycles before the stabilized state is obtained. The basis of this technique is to construct a displacement function to describe the responses at all times (t) during a load cycle with period (T) [32].

A simplified DP600 model, with dimensions of 50 mm × 50 mm × 1.25 mm, is used to compare the simulation results of the static general and direct cyclic steps. As shown in Figure 9, the stabilized stress and strain values (black symbols) obtained from both analysis steps are almost identical for the same number of cycles. However, the calculation time used for the direct cyclic step is less than that of the static general step. This advantage becomes more obvious as the complexity of the model and the number of cycles increase.

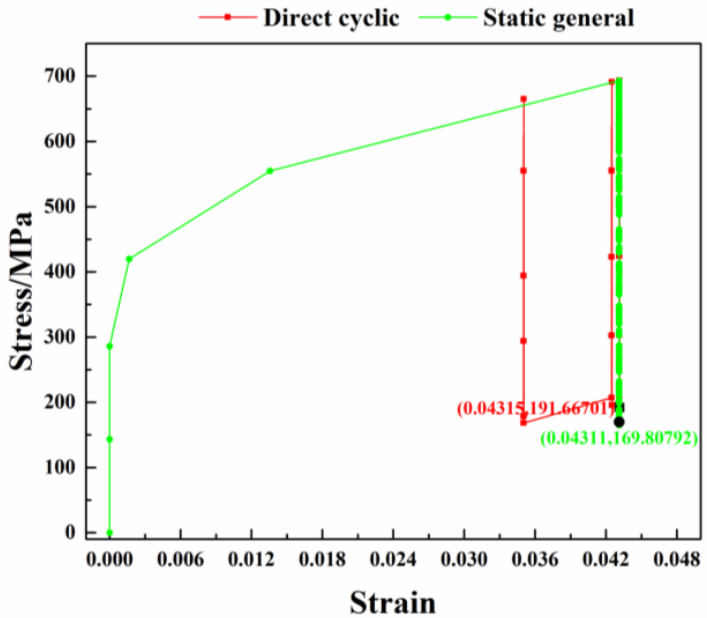

Figure 9. The stress-strain curves of two analysis steps.

4.5. Plastic Material Constitutive Models

The material constitutive models describe the evolution of the stress-strain relationship, which is the foundation for studying mechanical properties and service life [33]. The stress-plastic strain curve of the welded structure after the tensile experiment is shown in Figure 10. Generally, the material undergoes strain hardening when plastic deformation begins, thereby increasing the flow stress. The strain hardening behavior is usually affected by factors such as strain, temperature, and strain rate [34]. To precisely simulate the strain hardening behavior of the material, reliable plastic material constitutive models are established to describe the flow stress of material in a wide range of temperatures and strain rates.

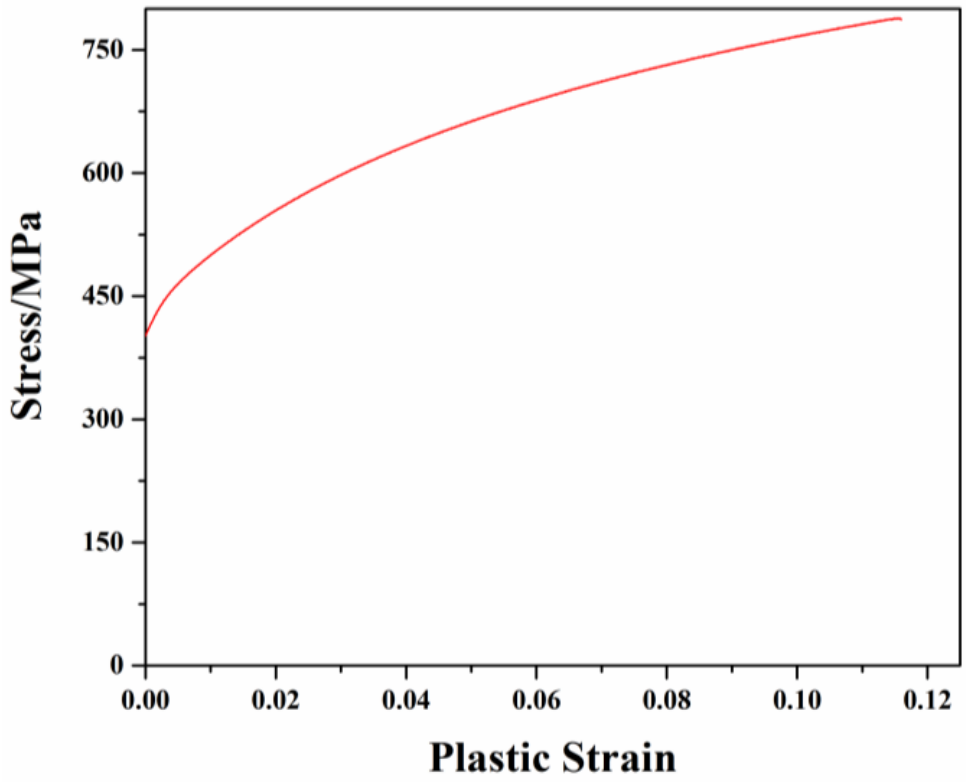

Figure 10. Tensile stress-plastic strain curve.

The Hollomon model is one of the classical plastic material constitutive models used to describe strain hardening behavior. It represents the relationship between stress and plastic strain and has long served as a model of the strain hardening behavior of many engineering metals and alloys [35].

$$\sigma = K\varepsilon^n \tag{11}$$

where σ is the stress (MPa), K is the hardening constant, ε is the plastic strain and n is the hardening exponent. These values depend on the materials used.

The mechanical properties change significantly for most materials, especially metals, with temperature and strain rate differences. To describe not only the strain hardening effect but also to fully consider the temperature softening and strain rate hardening effect of the flow stress, the Johnson-Cook model is used [36]:

$$\sigma = (A + B\varepsilon^n)(1 - T^{*m})\left[1 + Cln(1 + \frac{\dot{\varepsilon}}{\dot{\varepsilon}_0})\right] \tag{12}$$

$$T^* = \frac{T - T_r}{T_m - T_r} \tag{13}$$

where σ is the stress (MPa), ε is the plastic strain, T is the experimental temperature (°C), T_m is the melting point of the metal (°C), T_r is the room temperature (°C), ε is the equivalent plastic strain rate, ε_0 is the strain rate reference value, and A, B, C, m and n are the material parameters.

In addition to the most used models in engineering (Hollomon model) and finite element software (Johnson-Cook model), models related to the three factors (strain, temperature and strain rate) that influence strain hardening behavior are discussed in this paper. Various plastic material constitutive models are used to predict the residual stress distribution after laser welding. In addition, the effects of laser welding residual stress on low-cycle fatigue residual stress are further analyzed. Five models related to the strain hardening phenomena (named strain models) are used to describe the plastic flow behaviors of material at a fixed temperature and strain rate. Four models related to the temperature softening effect (named temperature models) describe the effects of temperature on plastic flow behaviors and are coupled with the same strain model. Three models related to the strain rate hardening effect (named strain rate models) describe the influences of strain rate on plastic flow behaviors and are coupled with the same strain model. The equations and parameters are in Tables 3–8. In Abaqus, different plastic material constitutive models can be defined through the UHARD subroutine.

Table 3. Equations of strain models.

Ludwik Model	$\sigma = \sigma_0 + K\varepsilon^n$	(14)
Voce Model	$\sigma = \sigma_0 + K[1 - \exp(-n\varepsilon)]$	(15)
Modified Ludwik Model	$\sigma = \sigma_0 + K_1\varepsilon^n + K_2\varepsilon + A$	(16)
Modified Voce Model	$\sigma = \sigma_0 + K_1[1 - \exp(-n\varepsilon)] + K_2\varepsilon$	(17)
Ludwik-Voce Model	$\sigma = \omega(\sigma_0 + K_1\varepsilon^{n_1}) + (1 - \omega)\{\sigma_0 + K_2[1 - \exp(-n_2\varepsilon)]\}$	(18)

Table 4. Parameters of strain models in this paper.

Parameters	σ_0	K	K_1	K_2	n	n_1	n_2	A
Ludwik Model	400	1244.24			0.53			
Voce Model	400	409.64			21.55			
Modified Ludwik Model	400		−33,610.91	1690.26	−0.001			3395.02
Modified Voce Model	400		189.60	1777.74	51.11			
Ludwik-Voce Model	400		89.78	506.11		5.02×10^{-11}	18.52	

Table 5. Equations of temperature models.

Khan Model	$F(T) = \left(\frac{T_m - T}{T_m - T_r}\right)^m$	(19)
Proposed Model	$F(T) = (1 - AT^{*m_1})^{m_2}$	(20)
Polynomial Model	$F(T) = A + BT + CT^2 + DT^3$	(21)

Table 6. Parameters of temperature models in this paper.

Parameters	Khan Model	Proposed Model	Polynomial Model
m	1.49		
m_1		3.24	
m_2		1.68	
A		6.54	0.89
B			1.13×10^{-3}
C			-4.02×10^{-6}
D			1.87×10^{-9}

Table 7. Equations of strain rate models.

Strain Rate Model	$G\left(\dot{\bar{\varepsilon}}\right) = 1 + \mathrm{Ash}\left[\frac{1}{2}\left(\frac{\dot{\bar{\varepsilon}}}{\dot{\bar{\varepsilon}}_0}\right)^n\right]$	(22)
Modified Strain Rate Model	$G\left(\dot{\bar{\varepsilon}}\right) = 1 + \mathrm{Ash}\left[\frac{1}{2}\left(\frac{\dot{\bar{\varepsilon}}}{\dot{\bar{\varepsilon}}_0}\right)^n + A\right]$	(23)
	$\mathrm{Ash}(x) = \ln(x + \sqrt{1 + x^2})$	(24)

Table 8. Parameters of strain rate models in this paper.

Parameters	n	A
Strain Rate Model	0.046	
Modified Strain Rate Model	0.084	−0.448

Two kinds of strain models are widely used for DP steels. One is the power law, such as the Ludwik Model [37]. It is suitable to describe the strain hardening capacity of martensite in steels combined with a strong hardening effect. The other is the saturation model, such as the Voce Model [38]. Contrary to the Ludwick Model, the Voce Model is used to describe material recovery (hardening with saturation plateau), such as the plastic flow of ferrite. Because the Ludwik Model is insufficient to describe plastic flow behavior and strain hardening at low strain values, the Modified Ludwik Model is proposed. Similarly, because the Voce Model is applicable only at high temperatures, the Modified Voce Model is proposed. The Ludwik-Voce Model is established which is better for simulating the stress change after the strain value of 0.2. It is a combination of the Ludwik Model and the Voce Model. In the Ludwik-Voce Model, ω is the proportion of martensite that changes in the welding process and is difficult to measure. The martensite in DP600 generally has a volume fraction from 10% to 20%, so the maximum value (20%) has been considered for simulations in this paper. The Ludwik-Voce Model is suitable for larger plastic strain range simulations. In equations, the yield strength is shown by a stress factor (σ_0), and K, K_1, K_2, n, n_1, n_2 and A are material parameters. The fitting curves are shown in Figure 11.

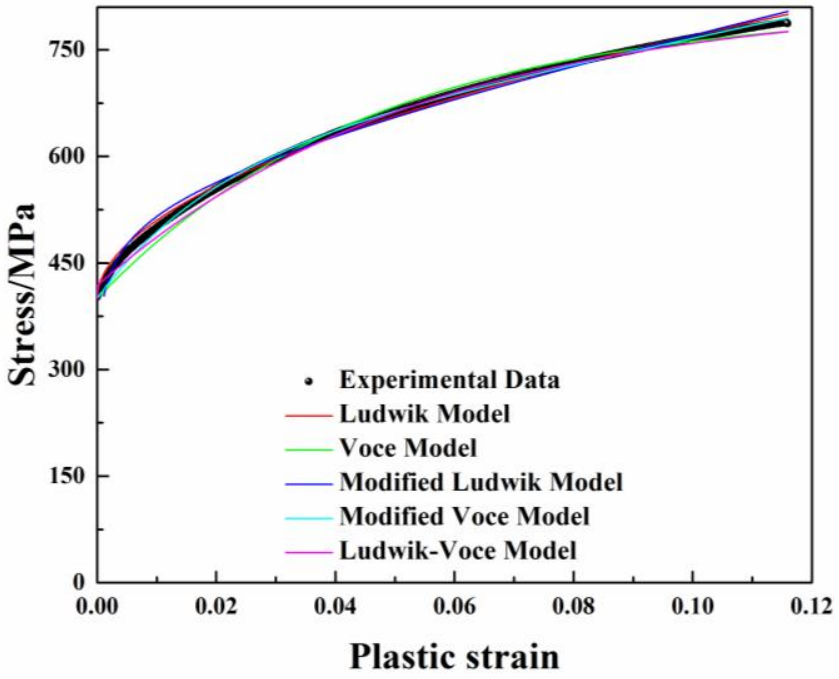

Figure 11. Experimental data and fitting curves of strain models.

When the temperature increases, the yield strength of DP600 decreases. During the laser welding process, the temperature changes rapidly due to the action of the laser heat source. Because low-cycle fatigue is performed at room temperature, only the effects of temperature models on residual stress during laser welding are discussed. The following models represent some forms of temperature softening factors, F(T), by setting $F(T_r) = 1$. According to the references [39], the experimental data of F(T) at different temperatures are known. The Khan Model [40] can only describe the temperature softening trend. The Polynomial Model is suitable for describing the fit of the temperature from 100 to 700 °C. The Proposed Model is proposed in this paper based on the temperature term of the Johnson-Cook model. It can be viewed as a more general temperature form of the Johnson-Cook model and can be better fitted to experimental data from room temperature up to 1000 °C. A, B, C, D, m, m_1 and m_2 are material parameters in equations. The fitting curves are shown in Figure 12.

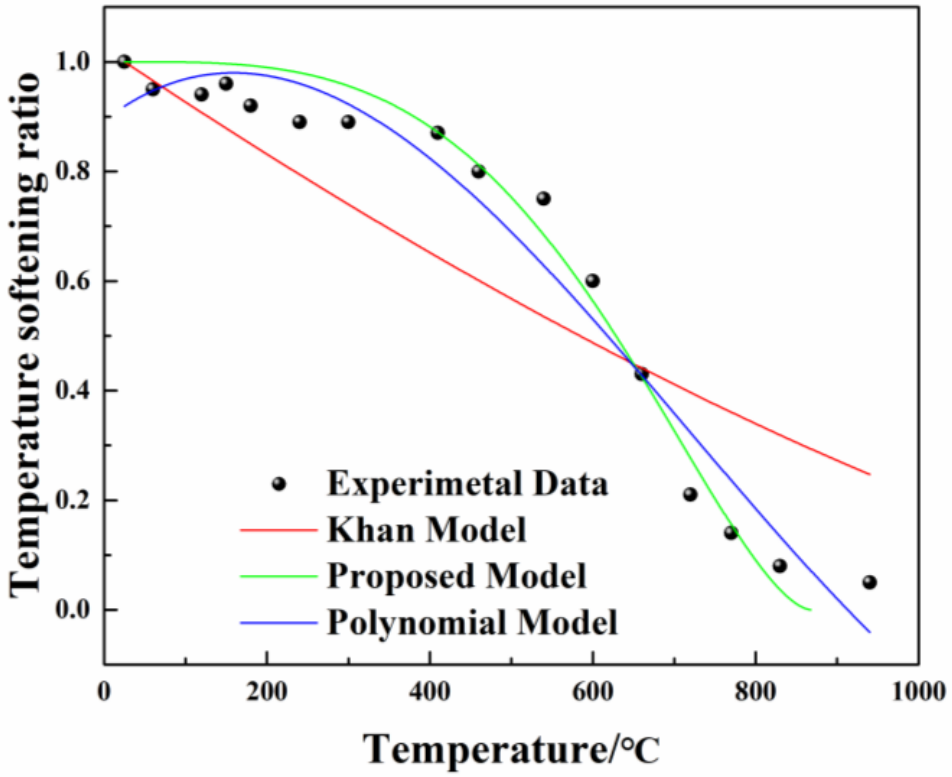

Figure 12. Experimental data and fitting curves of temperature models.

When the strain rate increases, the yield strength of DP600 increases. The following models show available forms of strain rate hardening factors $G\left(\dot{\bar{\varepsilon}}\right)$ by setting G(0.002) = 1. The yield stress under different strain rates can be obtained by reference [17]. The Strain Rate Model has been proposed by Gavrus [41]. It describe strain hardening behavior from low to high strain rate. A Modified Strain Rate Model is proposed to improve the fitting effect in this paper. In equations, A and n are material parameters. The fitting curves are shown in Figure 13.

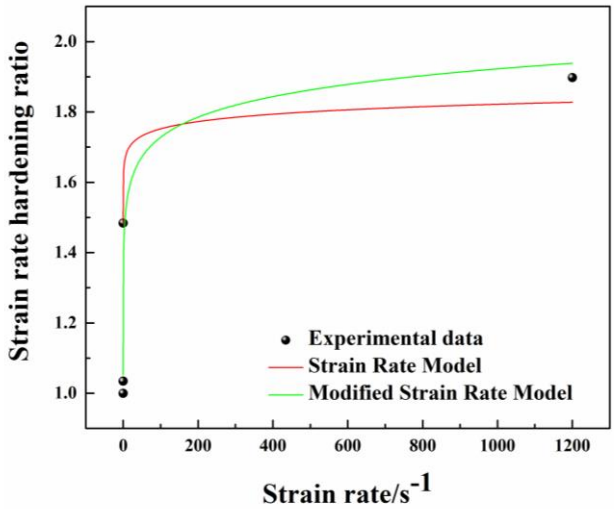

Figure 13. Experimental data and fitting curves of strain rate models.

5. Results and Discussions

5.1. Simulation Results

Figure 14 shows the laser welding residual stress curves along the longitudinal and transversal directions for plastic material constitutive models. The laser welding residual stress in both experiment and simulation is measured until the welded structure cools to room temperature. As observed, the profiles are approximately symmetric for all constitutive models. Laser welding residual stress is different when using different models. A small difference between models can result in a big difference in simulation results. In strain models (Figure 14a,b), regardless of longitudinal or transversal direction, the laser welding residual stress of the Modified Ludwik Model is higher than in other models. Because the Modified Ludwik Model is based on the Ludwik Model by adding terms of "$K_2\varepsilon + A$", these terms increase the hardening effect of martensite contents on the model, which in turn raises laser welding residual stress. The higher the martensite contents, the higher the laser welding residual stress [42]. In temperature models (Figure 14c,d), laser welding residual stress differences among different models are found. It shows that the differences in laser welding residual stress of 0 to 5 mm along the longitudinal direction are more significant than that of 5 to 10 mm. This is because the change of temperature fields in the later period of laser welding is greater than in the earlier period. In the later period, the temperature field is influenced by two main factors: the heat source and the ambient temperature and the temperature change of the molten metal during solidification [43]. Therefore, laser welding residual stress of 0 to 5 mm along the longitudinal direction has a large fluctuation. Moreover, it can also be found that the Without Temperature Model increases laser welding residual stress, indicating that temperature influences laser welding residual stress. In strain rate models (Figure 14e,f), it can be seen that laser welding residual stress, along both longitudinal and transversal directions considering the strain rate influence, is different from the results without considering the strain rate influence. Differences around 140 MPa of laser welding residual stress are found near the weld zone. Laser welding residual stress significantly decreases considering the strain rate influence, indicating that DP600 is a strain rate sensitive material, and the strain rate significantly influences laser welding residual stress [44]. The impact of strain rate on laser welding residual stress is larger near the weld zone. As the distance from the weld zone increases, the influence gradually becomes small. Furthermore, no matter which model is used, the peak of laser welding residual stress along the transversal direction (Figure 14b,d,f) is near the heat-affected zone with a peak value of around 210 to 290 MPa. This is because the welded structure expands to varying degrees during the laser welding process due to the non-uniform temperature field. The farther away from the weld, the less effect of thermal action. The molten metal gradually solidifies and shrinks when the heat source moves

away from the middle of the weld during the cooling process. The higher cooling rate refines the microstructure and gives the heat-affected zone a higher strength against the restraining effect, thus generating higher tensile residual stress [45].

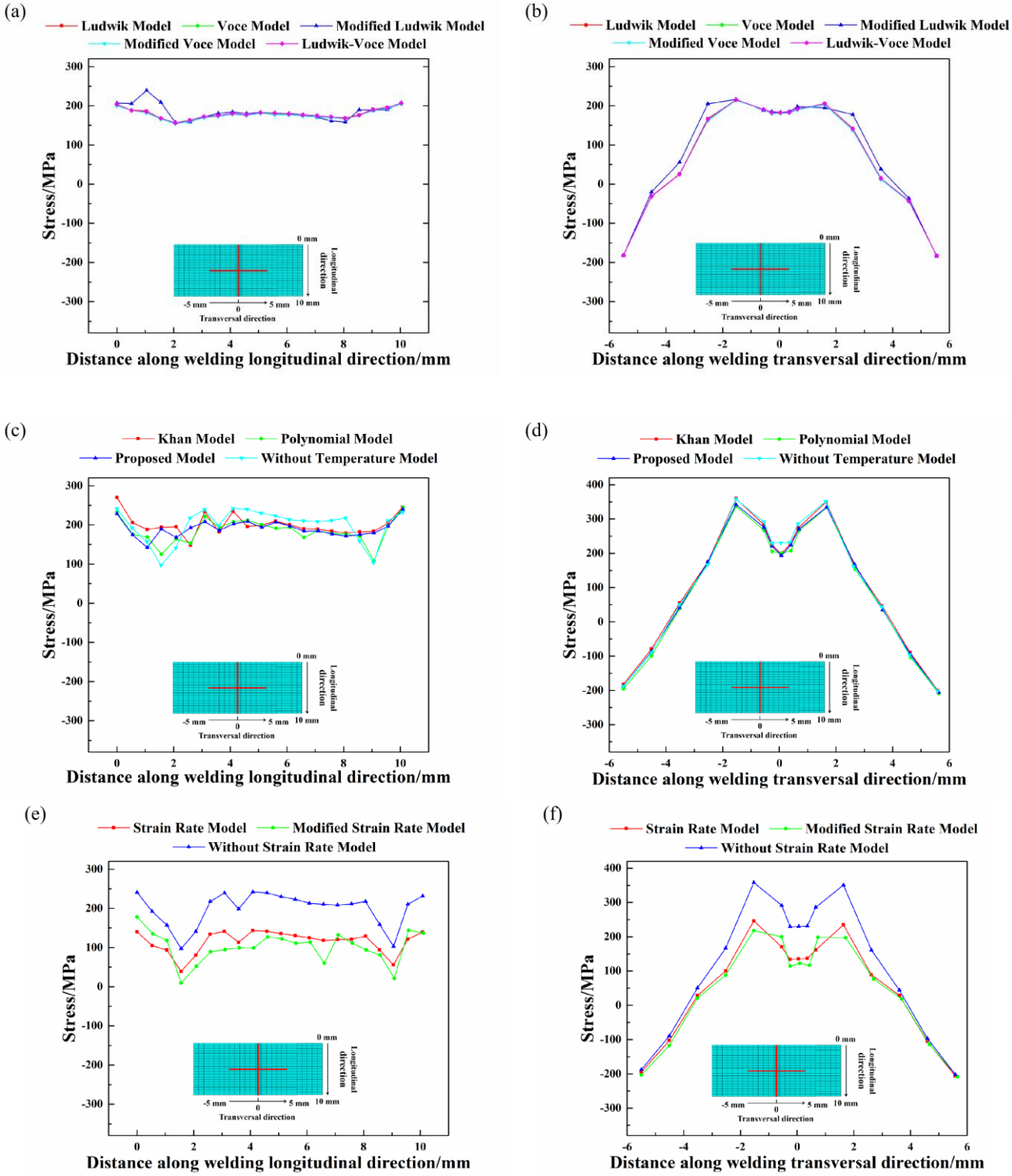

Figure 14. Laser welding residual stress for (**a**) longitudinal for strain models, (**b**) transversal for strain models, (**c**) longitudinal for temperature models, (**d**) transversal for temperature models, (**e**) longitudinal for strain rate models, (**f**) transversal for strain rate models.

The laser welding residual stress results are employed as the predefined fields in simulations for the low-cycle fatigue residual stress. Figure 15 shows the low-cycle fatigue residual stress curves along the longitudinal and transversal directions for experimental data. Due to the 0.1 mm gap in the welded structure, the centers of the two base metals are not on the same plane. One end of the welded structure is fixed while the other is loaded with cyclic loading, so low-cycle fatigue residual stress profiles along the transversal direction are asymmetric. Low-cycle fatigue residual stress positively correlates to the laser welding residual stress. In strain models (Figure 15a,b), the low-cycle fatigue residual stress is significantly lower in the Ludwik and Voce models compared to the Ludwik-Voce Model, especially in the Voce Model. It can also be seen from Figure 15b that the deformation calculated using the Voce Model is larger. It is because the Voce Model is used to describe the plastic flow of the ferrite. The martensite content increases when the welded structure is subjected to cyclic loading. Martensite compresses the surrounding ferrite matrix and creates new dislocation. Because the ferrite content of the welded structure is larger than the martensite, the Voce Model has a more significant effect on low-cycle fatigue residual stress and deformation than the Ludwik Model. In strain rate models (Figure 15c,d), it can be seen that low-cycle fatigue residual stress considering the strain rate influence, is lower than the results without considering the strain rate influence of around 80 MPa near the weld zone. Low-cycle fatigue residual stress along the transversal direction is found to increase by about 80 MPa in the weld center but almost the same at the beginning and end of the path. The strain rate significantly affects low-cycle fatigue residual stress, especially near the weld zone. Furthermore, low-cycle fatigue residual stress along the longitudinal direction is higher on the two sides and lower in the weld center in all models (Figure 15a,c). While laser welding residual stress is mainly caused by thermal variation, low-cycle fatigue residual stress is produced by the plastic deformation during cyclic loading [46]. When only one end of the welded structure is subjected to cyclic loading, deformation on the two sides is larger than the weld center. The microstructure changes and the crystal grains elongate along the direction of maximum deformation. Thus, low-cycle fatigue residual stress is higher on the two sides and lower in the center. Let us focus on the influence of temperature and strain rate on the plastic strain and yield strength and how temperature and strain rate play essential roles in dictating residual stress. Plastic strain is the result of the accumulation of dislocation motions in the crystal [47]. It is a function of material responses to cyclic loading [48]. The yield strength of the material is dependent on the change of temperature and strain rate as a temperature softening effect and a strain rate hardening effect during laser welding and low-cycle fatigue. The higher the temperature or the lower the strain rate, the lower the yield strength. In Equation (12), if the temperature coefficient m is more than 1, the softening effect increases with temperature. If $0 < m < 1$, the softening effect decreases with temperature [49]. When the material begins plastic deformation, if the influence of temperature and strain rate change on the residual stress is ignored, the simulation results will differ from the experimental data. The deviation will rise as the temperature and strain rate changing range increases.

The evolution of residual stress after 1, 2, 100 and 500 cycles is shown in Figure 16. The figure shows that residual stress relaxes in the weld and heat-affected zone. The relaxation occurs immediately after the first cycle and its amount depends on the magnitude of the cyclic loading. Then, the relaxation gradually remains stable. Using the Ludwik-Voce Model, the Proposed Model, and the Modified Strain Rate Model as examples, the relationship between laser welding and low-cycle fatigue residual stress can be analyzed. Figure 17 shows the laser welding and low-cycle fatigue residual stress curves along the longitudinal and transversal directions for three models. Redistribution of low-cycle fatigue residual stress and local stress reduction is found in the weld and heat-affected zone. This phenomenon is known as stress relaxation. The welded structure has cyclic loading applied at one end. The cyclic responses inside the welded structure affect residual stress when the loading superposes residual stress. Localized plastic deformation occurs when the stress in the weld and the heat-affected zone exceeds the yield strength. The welded structure

experiences secondary deformation when cyclic loading at the right end is removed. The original deformation of the welded structure is released by plastic deformation. As a result, residual stress redistributes and locally relaxes. The calculations of fatigue properties without considering residual stress relaxation may lead to inaccurate results [50].

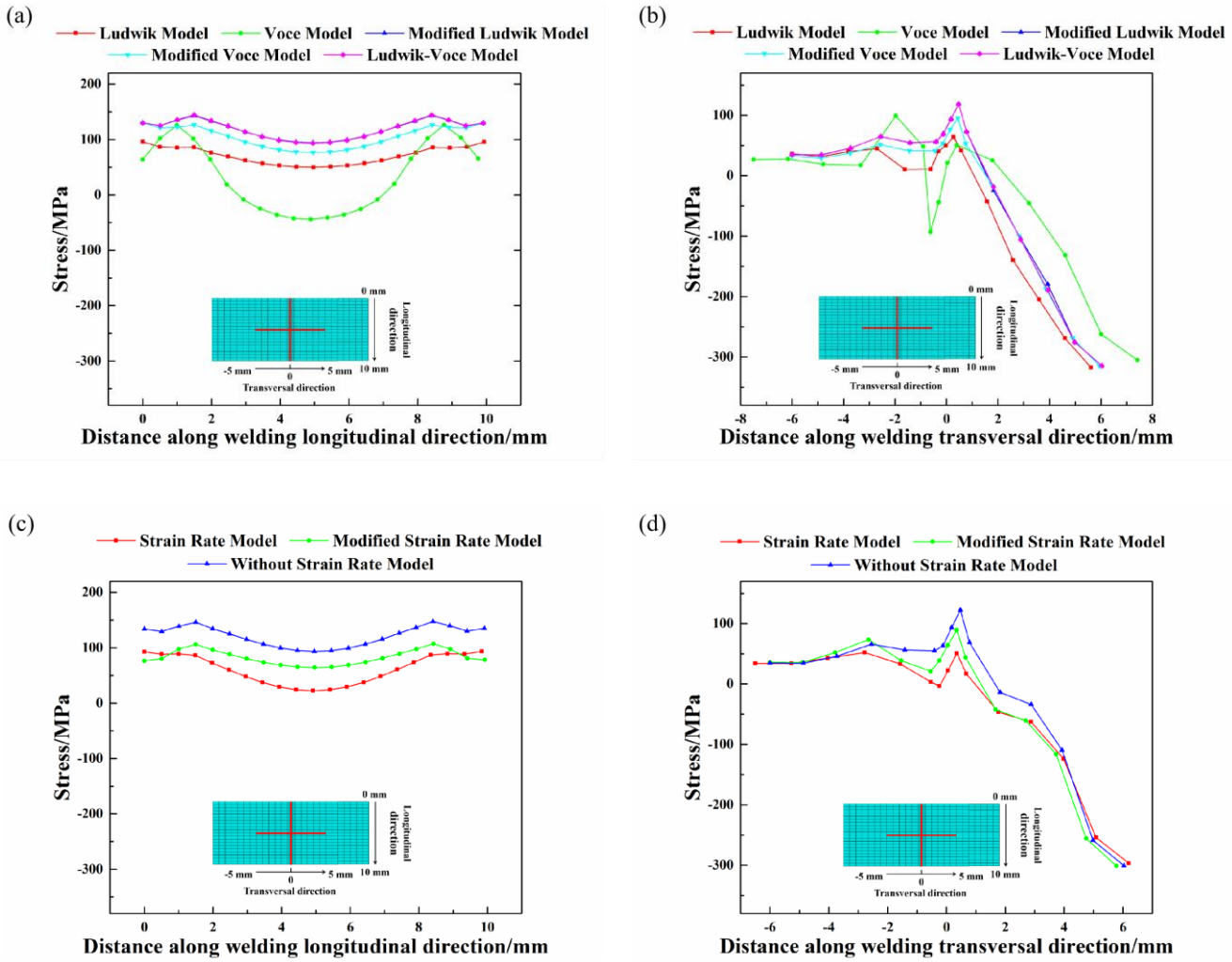

Figure 15. Low-cycle fatigue residual stress for (**a**) longitudinal for strain models, (**b**) transversal for strain models, (**c**) longitudinal for strain rate models, (**d**) transversal for strain rate models.

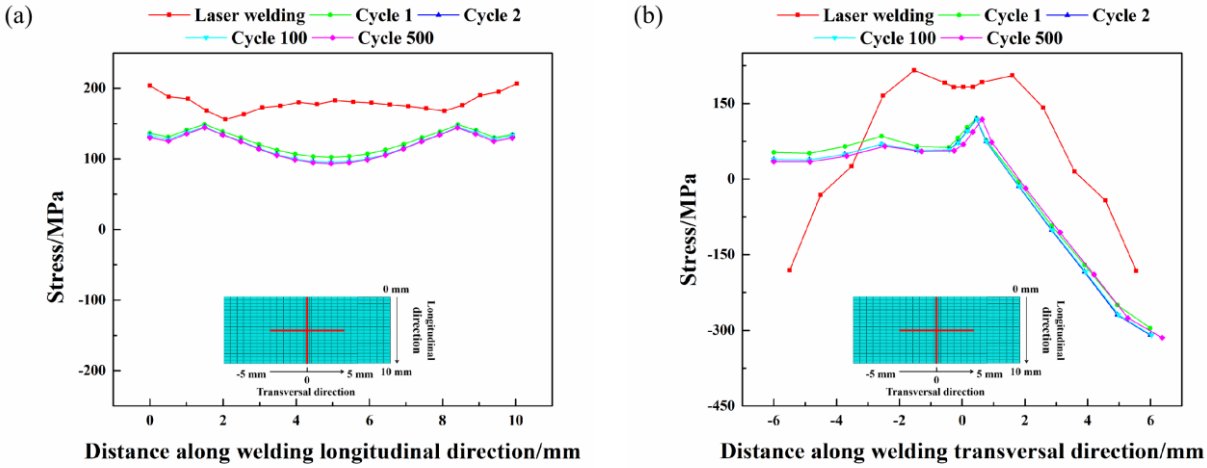

Figure 16. Evolution of residual stress for (**a**) longitudinal, (**b**) transversal.

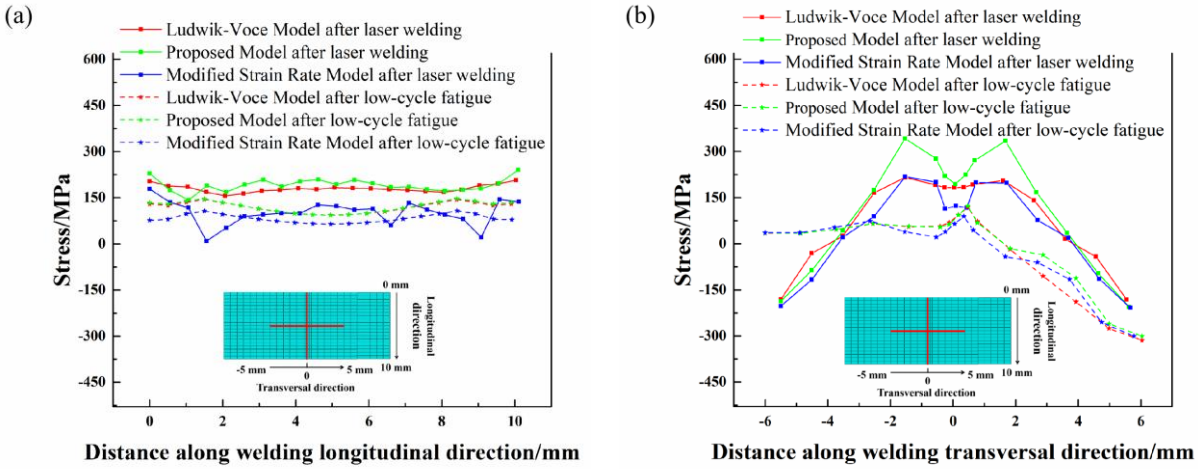

Figure 17. Laser welding and low-cycle fatigue residual stress for (**a**) longitudinal, (**b**) transversal.

Figure 18 shows the low-cycle fatigue residual stress curves along the longitudinal and transversal directions of the base metal. It should be noted that the values are almost the same. The average value of low-cycle fatigue residual stress is about 120 MPa. The low-cycle fatigue residual stress of welded structure is higher than that of the base metal. The welded structure first experiences residual stress due to the thermal effect. Although the residual stress is reduced due to relaxation behaviour during the low-cycle fatigue, there is still residual stress due to plastic deformation. Therefore, the residual stress of the welded structure after low-cycle fatigue is higher than that of the base metal. Furthermore, the phenomenon indicates that laser welding generates high residual stress and increases low-cycle fatigue residual stress. It requires post-treatment after laser welding to eliminate residual stress and reduce the adverse effects of residual stress.

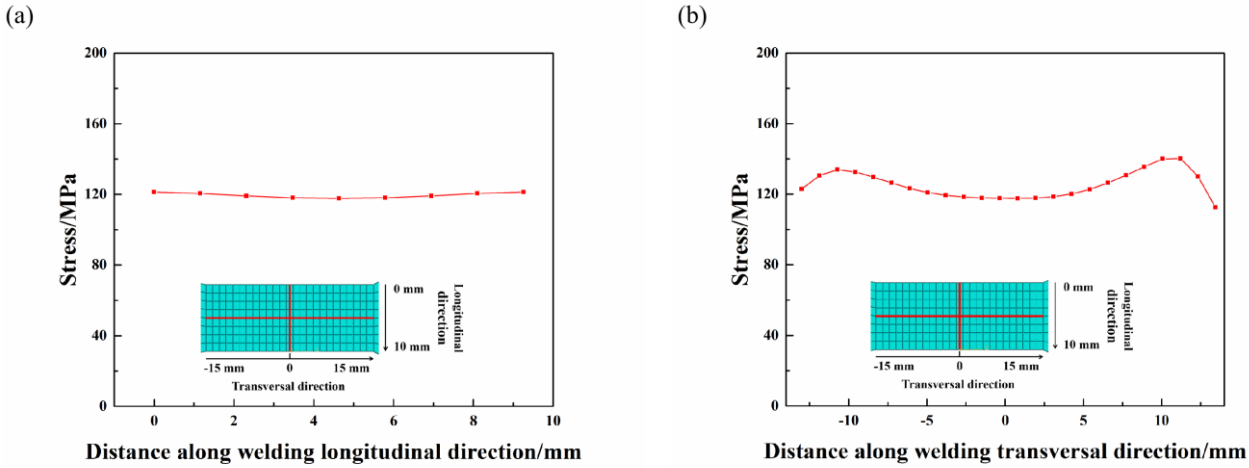

Figure 18. Low-cycle fatigue residual stress of the base metal for (**a**) longitudinal, (**b**) transversal.

5.2. Comparison of Experiment and Simulation

An example is used to validate simulation results by comparing them with the experimental data. Figure 19 shows the low-cycle fatigue residual stress curves along the longitudinal direction through simulation and experiment. All simulated process parameters and other conditions are identical to those in the experiment. The findings of the simulation and experiment show a fair degree of agreement. Figure 20 shows the cyclic stress-strain curves of the simulation and experiment. The stabilized stress and strain values (black symbols) are almost identical.

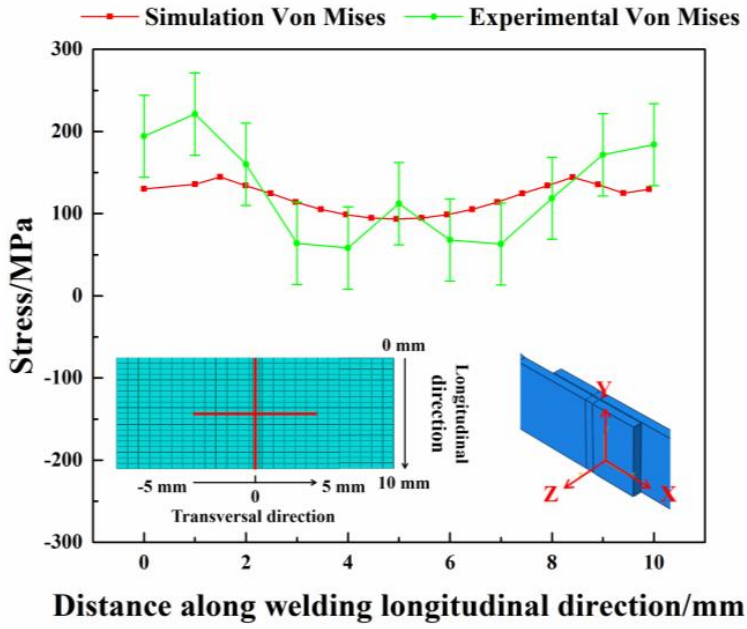

Figure 19. Low-cycle fatigue residual stress by simulation and experiment.

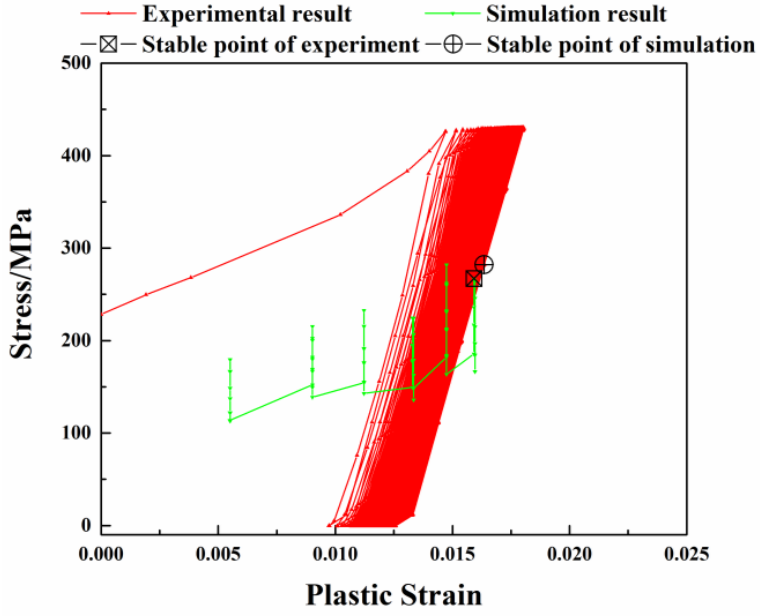

Figure 20. Simulation and experimental cyclic stress-strain curves.

6. Conclusions

In this study, the sequential-coupled thermo-mechanical model and the direct cyclic technique are used for laser welding and low-cycle fatigue simulations to analyze the relationship between residual stress and fatigue properties of DP600. Different plastic material constitutive models describing the strain hardening, temperature softening and strain hardening effect are established. Through comparison with the experimental data of the neutron diffraction method, constitutive models are proved to be useful in predicting residual stress, and the laser welding residual stress has influences on the low-cycle fatigue residual stress. The following conclusions can be drawn:

(1) The conical heat source with Gaussian distribution heat source model and plastic material constitutive models are used to simulate laser welding residual stress. The laser welding residual stress varies under different constitutive models and reaches the maximum in the heat-affected zone.
(2) The magnitude of laser welding residual stress significantly influences low-cycle fatigue residual stress. The larger the laser welding residual stress is, the larger the low-cycle fatigue residual stress is. In all models, low-cycle fatigue residual stress along the longitudinal direction is higher on the two sides and lower in the center.
(3) Low-cycle fatigue residual stress of the welded structure is higher than that of the base metal, indicating that laser welding residual stress increases low-cycle fatigue residual stress. The structure requires post-treatment after laser welding to eliminate residual stress and reduce the adverse effects of residual stress.
(4) Low-cycle fatigue residual stress of the welded structure redistributes and locally relaxes in the weld and heat-affected zone after the first cycle and then gradually remains stable.
(5) Comparing the residual stress obtained from simulation and experiment, it can be inferred that the simulation results are close to the experimental data. In subsequent studies, process parameters and models can be optimized to reduce errors better.

Author Contributions: M.L.: Writing-Original Draft, Writing-Review and Editing. A.K.-H.: Writing-Review and Editing, Supervision. B.M.: Writing-Review and Editing. All authors have read and agreed to the published version of the manuscript.

Funding: This research received no external funding.

Institutional Review Board Statement: Not applicable.

Informed Consent Statement: Not applicable.

Data Availability Statement: Data is contained within the article.

Acknowledgments: The work is supported by China Scholarship Council (CSC), INSA de Rennes and Laboratory of Digital Sciences of Nantes (LS2N). Also, thanks to the Institut Laue Langevin (ILL) with the collaboration of Sandra Cabeza.

Conflicts of Interest: The authors declare that they have no conflict of interest concerning the publication of this manuscript.

References

1. Zhang, Y.; You, D.; Gao, X.; Zhang, N.; Gao, P.P. Welding defects detection based on deep learning with multiple optical sensors during disk laser welding of thick plates. *J. Manuf. Syst.* **2019**, *51*, 87–94. [CrossRef]
2. Yunlian, Q.; Ju, D.; Quan, H.; Liying, Z. Electron beam welding, laser beam welding and gas tungsten arc welding of titanium sheet. *Mater. Sci. Eng. A* **2000**, *280*, 177–181. [CrossRef]
3. Xue, X.; Pereira, A.B.; Amorim, J.; Liao, J. Effects of pulsed Nd: YAG laser welding parameters on penetration and microstructure characterization of a DP1000 steel butt joint. *Metals* **2017**, *7*, 292. [CrossRef]
4. Fernandes, F.; Oliveira, D.; Pereira, A. Optimal parameters for laser welding of advanced high-strength steels used in the automotive industry. *Procedia Manuf.* **2017**, *13*, 219–226. [CrossRef]
5. Available online: http://www.laserline.com (accessed on 27 October 2022).
6. Wang, X.; Meng, Q.; Hu, W. Fatigue life prediction for butt-welded joints considering weld-induced residual stresses and initial damage, relaxation of residual stress, and elasto-plastic fatigue damage. *Fatigue Fract. Eng. Mater. Struct.* **2019**, *42*, 1373–1386. [CrossRef]
7. Marciszko, M. Diffraction Study of Mechanical Properties and Residual Stresses Resulting from Surface Processing of Polycrystalline Materials. Ph.D. Thesis, Ecole Nationale Supérieure D'arts et Métiers-ENSAM, Krakow, Poland, 2013.
8. Viktor, H. *Structural and Residual Stress Analysis by Nondestructive Methods: Evaluation-Application-Assessment*; Elsevier: Amsterdam, The Netherlands, 1997.
9. Zhiping, Q.; Zesheng, Z.; Lei, W. Numerical analysis methods of structural fatigue and fracture problems. *Contact Fract. Mech.* **2018**, *12*, 235.
10. Rong, Y.; Lei, T.; Xu, J.; Huang, Y.; Wang, C. Residual stress modelling in laser welding marine steel EH36 considering a thermodynamics-based solid phase transformation. *Int. J. Mech. Sci.* **2018**, *146*, 180–190. [CrossRef]

11. Amit, K.; Pandey, C. Autogenous laser-welded dissimilar joint of ferritic/martensitic P92 steel and Inconel 617 alloy: Mechanism, microstructure, and mechanical properties. *Arch. Civ. Mech. Eng.* **2022**, *22*, 39.
12. Kumar, R.; Dey, H.C.; Pradhan, A.K.; Albert, S.K.; Thakre, J.G.; Mahapatra, M.M.; Pandey, C. Numerical and experimental investigation on distribution of residual stress and the influence of heat treatment in multi-pass dissimilar welded rotor joint of alloy 617/10Cr steel. *Int. J. Press. Vessel. Pip.* **2022**, *199*, 104715. [CrossRef]
13. Nassiraei, H.; Rezadoost, P. Stress concentration factors in tubular T/Y-joints strengthened with FRP subjected to compressive load in offshore structures. *Int. J. Fatigue* **2020**, *140*, 105719. [CrossRef]
14. Nassiraei, H.; Rezadoost, P. SCFs in tubular X-connections retrofitted with FRP under in-plane bending load. *Compos. Struct.* **2021**, *274*, 114314. [CrossRef]
15. Nassiraei, H.; Rezadoost, P. Development of a probability distribution model for the SCFs in tubular X-connections retrofitted with FRP. *Structures* **2022**, *36*, 233–247. [CrossRef]
16. Bassindale, C.; Miller, R.; Wang, X. Effect of single initial overload and mean load on the low-cycle fatigue life of normalized 300 M alloy steel. *Int. J. Fatigue* **2020**, *130*, 105273. [CrossRef]
17. Mihaliková, M.; Zgodavová, K.; Bober, P.; Špegárová, A. The performance of CR180IF and DP600 laser welded steel sheets under different strain rates. *Materials* **2021**, *14*, 1553. [CrossRef]
18. Farabi, N.; Chen, D.; Li, J.; Zhou, Y.; Dong, S. Microstructure and mechanical properties of laser welded DP600 steel joints. *Mater. Sci. Eng. A* **2010**, *527*, 1215–1222. [CrossRef]
19. McCallum, B. Characterization of DP600 Steel Subject to Electrohydraulic Forming. Master's Thesis, University of Windsor, Windsor, ON, Canada, 2014.
20. *ASTM E606*; Standard Practice for Strain-Controlled Fatigue Testing. ASTM: West Conshohocken, PE, USA, 1998; Volume 3.
21. Guo, J.; Fu, H.; Pan, B.; Kang, R. Recent progress of residual stress measurement methods: A review. *Chin. J. Aeronaut.* **2021**, *34*, 54–78. [CrossRef]
22. Bacon, G.E.; Lonsdale, K. Neutron diffraction. *Rep. Prog. Phys.* **1953**, *16*, 1. [CrossRef]
23. Avettand-Fènoël, M.-N.; Sapanathan, T.; Pirling, T.; Racineux, G.; Simar, A.; Drezet, J.-M. Investigation of residual stresses in planar dissimilar magnetic pulse welds by neutron diffraction. *J. Manuf. Process.* **2021**, *68*, 1758–1766. [CrossRef]
24. Noyan, C.; Cohen, J.B. *Residual Stress: Measurement by Diffraction and Interpretation*; Springer: Berlin/Heidelberg, Germany, 2013.
25. Kouadri-Henni, A.; Seang, C.; Malard, B.; Klosek, V. Residual stresses induced by laser welding process in the case of a dual-phase steel DP600: Simulation and experimental approaches. *Mater. Des.* **2017**, *123*, 89–102. [CrossRef]
26. Brown, D.; Bernardin, J.; Carpenter, J.; Clausen, B.; Spernjak, D.; Thompson, J. Neutron diffraction measurements of residual stress in additively manufactured stainless steel. *Mater. Sci. Eng. A* **2016**, *678*, 291–298. [CrossRef]
27. Zhu, X.-K.; Leis, B.N. Average shear stress yield criterion and its application to plastic collapse analysis of pipelines. *Int. J. Press. Vessel. Pip.* **2006**, *83*, 663–671. [CrossRef]
28. Seang, C.; David, A.; Ragneau, E. Nd: YAG laser welding of sheet metal assembly: Transformation induced volume strain affect on elastoplastic model. *Phys. Procedia* **2013**, *41*, 448–459. [CrossRef]
29. Seang, C.; Kouadri, A.D.; Ragneau, E. (Optimization of thermal and discretization parameters in laser welding simulation Nd: YAG applied for shin plate transparent mode of DP600. *Int. J. Mech. Mechatron. Eng.* **2012**, *6*, 7–13.
30. Farias, R.; Teixeira, P.; Vilarinho, L. An efficient computational approach for heat source optimization in numerical simulations of arc welding processes. *J. Constr. Steel Res.* **2021**, *176*, 106382. [CrossRef]
31. Kik, T. Heat source models in numerical simulations of laser welding. *Materials* **2020**, *13*, 2653. [CrossRef]
32. Abaqus, I. *ABAQUS Analysis User's Manual, Volume II: Analysis*; Simulia: Johnston, RI, USA, 2007.
33. Chen, J.J.; Lian, C.W.; Lin, J.P. Validation of constitutive models for experimental stress-strain relationship of high-strength steel sheets under uniaxial tension. *Mater. Sci. Eng.* **2019**, *668*, 012013. [CrossRef]
34. Sener, B.; Yurci, M. Comparison of quasi-static constitutive equations and modeling of flow curves for austenitic 304 and ferritic 430 stainless steels. *Acta Phys. Pol. A* **2017**, *131*, 605–608. [CrossRef]
35. Mukarati, T.W.; Mostert, R.J.; Siyasiya, C.W. Development of a mathematical equation describing the strain hardening behaviour of metastable AISI 301 austenitic stainless steel. *Mater. Sci. Eng.* **2019**, *655*, 012008. [CrossRef]
36. Wang, X.; Huang, C.; Zou, B.; Liu, H.; Zhu, H.; Wang, J. Dynamic behavior and a modified Johnson-Cook constitutive model of Inconel 718 at high strain rate and elevated temperature. *Mater. Sci. Eng. A* **2013**, *580*, 385–390. [CrossRef]
37. Soussan, A.; Degallaix, S.; Magnin, T. Work-hardening behaviour of nitrogen-alloyed austenitic stainless steels. *Mater. Sci. Eng. A* **1991**, *142*, 169–176. [CrossRef]
38. Naderi, M.; Durrenberger, L.; Molinari, A.; Bleck, W. Constitutive relationships for 22MnB5 boron steel deformed isothermally at high temperatures. *Mater. Sci. Eng. A* **2008**, *478*, 130–139. [CrossRef]
39. Chen, J.; Young, B.; Uy, B. Behavior of high strength structural steel at elevated temperatures. *Eng. Struct.* **2006**, *132*, 1948–1954. [CrossRef]
40. Khan, A.S.; Suh, Y.S.; Kazmi, R. Quasi-static and dynamic loading responses and constitutive modeling of titanium alloys. *Int. J. Plast.* **2004**, *20*, 2233–2248. [CrossRef]
41. Adinel, G. Constitutive equation for description of metallic materials behavior during static and dynamic loadings taking into account important gradients of plastic deformation. *Key Eng. Mater.* **2012**, *504*, 697–702.

42. Berrahmoune, M.; Berveiller, S.; Inal, K.; Patoor, E. Delayed cracking in 301LN austenitic steel after deep drawing: Martensitic transformation and residual stress analysis. *Mater. Sci. Eng. A* **2006**, *438*, 262–266. [CrossRef]
43. Liu, M.; Ma, G.; Liu, D.; Yu, J.; Niu, F.; Wu, D. Microstructure and mechanical properties of aluminum alloy prepared by laser-arc hybrid additive manufacturing. *J. Laser Appl.* **2020**, *32*, 022052. [CrossRef]
44. Rahmaan, T.; Bardelcik, A.; Imbert, J.; Butcher, C.; Worswick, M. Effect of strain rate on flow stress and anisotropy of DP600, TRIP780, and AA5182-O sheet metal alloys. *Int. J. Impact Eng.* **2020**, *88*, 72–90. [CrossRef]
45. Derakhshan, E.D.; Yazdian, N.; Craft, B.; Smith, S.; Kovacevic, R. Numerical simulation and experimental validation of residual stress and welding distortion induced by laser-based welding processes of thin structural steel plates in butt joint configuration. *Opt. Laser Technol.* **2018**, *104*, 170–182. [CrossRef]
46. Fergani, O.; Shao, Y.; Lazoglu, I.; Liang, S.Y. Temperature effects on grinding residual stress. *Procedia CIRP* **2014**, *14*, 2–6. [CrossRef]
47. Babu, B.; Lindgren, L.-E. Dislocation density based model for plastic deformation and globularization of Ti-6Al-4V. *Int. J. Plast.* **2013**, *50*, 94–108. [CrossRef]
48. Wedage, A.M.P.; Morgenstern, N.R.; Chan, D.H. A strain rate dependent constitutive model for clays at residual strength. *Can. Geotech. J.* **1998**, *35*, 364–373. [CrossRef]
49. Song, B.; Sanborn, B. A modified Johnson—Cook model for dynamic response of metals with an explicit strain-and strain-rate-dependent adiabatic thermosoftening effect. *J. Dyn. Behav. Mater.* **2019**, *5*, 212–220. [CrossRef]
50. Chakherlou, T.N.; Yaghoobi, A. Numerical simulation of residual stress relaxation around a cold-expanded fastener hole under longitudinal cyclic loading using different kinematic hardening models. *Fatigue Fract. Eng. Mater. Struct.* **2010**, *33*, 740–751. [CrossRef]